Research Article

Hybrid Perovskite, CH$_3$NH$_3$PbI$_3$, for Solar Applications: An Experimental and Theoretical Analysis of Substitution in A and B Sites

Antonio Sánchez-Coronilla,[1] Javier Navas,[2] Juan Jesús Gallardo,[2] Elisa I. Martín,[3] Desireé De los Santos,[2] Norge C. Hernández,[4] Rodrigo Alcántara,[2] José Hidalgo Toledo,[1] and Concha Fernández-Lorenzo[2]

[1]*Departamento de Química Física, Facultad de Farmacia, Universidad de Sevilla, 41012 Sevilla, Spain*
[2]*Departamento de Química Física, Facultad de Ciencias, Universidad de Cádiz, Puerto Real, 11510 Cádiz, Spain*
[3]*Departamento de Ingeniería Química, Facultad de Química, Universidad de Sevilla, 41012 Sevilla, Spain*
[4]*Departamento de Física Aplicada I, Escuela Técnica Superior de Ingeniería Informática, Universidad de Sevilla, 41012 Sevilla, Spain*

Correspondence should be addressed to Antonio Sánchez-Coronilla; antsancor@us.es and Javier Navas; javier.navas@uca.es

The effect of the incorporation of NH$_4^+$ into the CH$_3$NH$_3^+$ sites of the tetragonal perovskite CH$_3$NH$_3$PbI$_3$ is analysed. Also, how it affects the introduction of Cd^{2+} cations into Pb^{2+} sites for a perovskite with 25 at.% of NH$_4^+$ is addressed. The incorporation of NH$_4^+$ into perovskite leads to a dramatic loss of crystallinity and to the presence of other phases. Moreover, the NH$_4$PbI$_3$ was not found. The less formation of perovskite when NH$_4^+$ is incorporated is due to geometrical factors and not changes in the chemical state bonding of the ions. Also, the samples where perovskite is formed show similar band gap values. A slight increase is observed for samples with $x = 0.5$ and 0.75. For the sample with $x = 1$, a drastic increase of the band gap is obtained. Periodic-DFT calculations agree with the experimental structural tendency when NH$_4^+$ is incorporated and the density of states analysis confirmed the experimental band gap. The perovskite with 25 at.% of NH$_4^+$ was selected for studying the effect of the concentration of Cd on the structural and electronic properties. The theoretical band gap values decreased with the Cd concentration where the narrowing of Cd s-states in the conduction band plays an important role.

1. Introduction

Organic-inorganic hybrid perovskite of the composition ABX$_3$ has recently attracted strong research interest because of its photovoltaic properties [1]. This simple structure consists of a network of corner-sharing BX$_6$ octahedra, where the B atom is a metal cation (usually Sn^{2+} or Pb^{2+}) and X is a monovalent anion, such as Cl$^-$, Br$^-$, or I$^-$. Also, the A cation is selected to neutralize the total charge and it can even be a molecule. In this case, the organic cation must fit into a rigid and relatively small cuboctahedral hole formed by the 12 nearest X atoms, thus, limiting the dimension of the selected molecule. The most common A cation is [CH$_3$NH$_3$]$^+$

(MA). In turn, perovskite solar cells have achieved a power conversion efficiency record higher than 20% [2]. The different components of the perovskite solar cells affect their conversion efficiency. Also, the effect of using mixtures of ions in the three positions of the perovskite (A, B, and X) has been analysed previously [3, 4]. For example, the substitution of I$^-$ with Cl$^-$ or Br$^-$ has been widely studied; and doping with inorganic cations such as Sn^{2+}, Sr^{2+}, or Ca^{2+} in Pb^{2+} sites has been analysed to understand its effect on optical and electronic properties [5–8].

Thus, this article shows the synthesis of organic-inorganic hybrid perovskite starting from MAPbI$_3$ and substituting the CH$_3$NH$_3^+$ cation by NH$_4^+$. Perovskites with the formula

$(A)_x(MA)_{1-x}PbI_3$ (x = 0.25; 0.50; 0.75; 1.00) were synthesized. These perovskites were characterized using X-ray fluorescence and CHNS technique for the elemental analysis, X-ray diffraction to determine the presence of the perovskite structure, X-ray photoelectron spectroscopy in order to analyse the chemical state bonding of the elements in the samples, and UV-vis spectroscopy for determining the optical properties and the band gap energy. Consequently, the presence of NH_4^+ affected the formation of the perovskite structure because distortions were produced in the structure. In turn, periodic density functional theory (DFT-periodic) calculations were performed to rationalize the experimental information for $(A)_x(MA)_{1-x}PbI_3$ (x = 0.25; 0.50; 0.75; 1.00). The theoretical results indicate that the $(A)_{0.25}(MA)_{0.75}PbI_3$ structure has an appropriate percentage of A^+ and MA^+ ions for being effective for its application in solar cells and was selected for the introduction of Cd^{2+} cations into Pb^{2+} sites. Thus, the increased concentration of Cd on the structural and electronic properties of $(A)_{0.25}(MA)_{0.75}Pb_{1-x}Cd_xI_3$ with x = 0.00, 0.25, 0.50, 0.75, and 1.00 was studied. In this regard, the theoretical results show that the theoretical band gap values decreased with the Cd concentration. In this sense, the narrowing of Cd s-states in the conduction band plays an important role.

2. Materials and Methods

2.1. Experimental Section. The synthesis of the perovskite phases was performed by the reaction of commercial PbI_2 and nominal amounts of CH_3NH_3I and commercial NH_4I. First, CH_3NH_3I was synthesized using the following procedure [6, 9, 10]: HI (57 wt% in water, 10 mL, 0.076 mol) and CH_3NH_2 (33 wt% in ethanol, 11.33 mL, 0.091 mol) were stirred in an ice bath for 2 h. Next, the mixture was evaporated at 50°C for 1 h, and CH_3NH_3I was obtained. Then, the solid was cleaned three times using Et_2O (purity ≥ 99.8%). On the other hand, for the synthesis of the perovskite phase PbI_2 (purity 99%, 1.153 g) was mixed with the corresponding stoichiometric amount of CH_3NH_3I and NH_4I to obtain nominal concentrations $(NH_4^+)/[(NH_4^+) + (CH_3NH_3^+)]$ of 0, 25, 50, 75, and 100 at.% in γ-butyrolactone (purity ≥ 99%, 2 mL) at 60°C for 18 h.

On the other hand, the elemental analysis was performed using two instrumental techniques. X-ray fluorescence (XRF) was performed to determine the amount of Pb and I using a sequential XRF spectrometer supplied by Bruker®, model Pioneer S4. The CHNS technique was used to obtain the amount of C, H, and N, using an elemental analyser supplied by Leco®, model CHNS932. To determine the crystalline phases in the samples, X-ray diffraction (XRD) was used. The patterns were recorded using a D8 Discover diffractometer supplied by Bruker with Cu-Kα radiation. The scan conditions were from 10 to 70° in 2θ with a resolution of 0.02°, 40 kV, and 40 mA. Moreover, X-ray photoelectron spectroscopy (XPS) was used to study the chemical bonding states and the chemical compositions of the samples. The spectra were obtained by using a Kratos® Axis UltraDLD spectrometer, with monochromated Al-Kα radiation (1486.6 eV) and a 20 eV pass energy. The binding

energy scale was given with an accuracy of 0.01 eV. Finally, the optical band gap (E_g) values were determined from diffuse reflectance UV-Vis (DR-UV-Vis) measurements. The spectra were collected by using a system assembled in our laboratory composed of an integrating sphere supplied by Spectra Tech®, a USB2000+ spectrometer supplied by Ocean Optics®, and a Xe lamp, model ASB-XE-175, supplied by Spectral Products®, as the illumination source.

2.2. Computational Framework. DFT-periodic calculations were performed using the Vienna Ab Initio Simulation Package (VASP) [11–14] with the projector-augmented wave (PAW) method [15, 16]. The number of plane waves in VASP was controlled by a cut-off energy, set in our calculations to E_{cut} = 500 eV to satisfactorily describe the system [11–16]. The electron exchange and correlation were treated within the generalized gradient approximation (GGA) [17]. In the case of GGA, Perdew-Burke-Ernzerhof (PBE) [17] functionals were used. Both the cell shape and atomic positions were optimized using a conjugate-gradient algorithm, where the iterative relaxation of atomic positions was stopped when the forces on the atoms were less than 0.01 eV/Å. Also, a Gaussian smearing with k_BT = 0.1365 eV was applied.

Perovskite tetragonal phase was characterized by the I4/mcm space group [17]. The tag KSPACING determined the number of k-points in the mesh. A value of 0.4 for sampling the Brillouin zone for perovskite bulk was enough to obtain negligible changes in the optimized cell parameters and energy. The resulting cell parameters were a = 8.912 Å and c = 12.707 Å for the tetragonal phase, in agreement with the experimental values (a = 8.874 Å, c = 12.671 Å) [17].

The $(MA)_4Pb_4I_{12}$ cell was optimized as a model for the tetragonal phase of perovskite. The A^+ ion substitutes the MA^+ ion and the most stable structures have been reported. Thus, the structures $(A)(MA)_3Pb_4I_{12}$, $(A)_2(MA)_2Pb_4I_{12}$, $(A)_3(MA)_1Pb_4I_{12}$, and $A_4Pb_4I_{12}$ were optimized. The incorporation of each proportion of Cd into the $(A)(MA)_3Pb_4I_{12}$ structure was performed in substitutional positions. The Cd atom substitutes the Pb atom in the perovskite structure taking into account the equivalent sites. Close attention was paid to the orientational disorder of MA within the tetragonal structure, reporting the most stable configuration for each doped structure, as reported elsewhere [6, 18, 19].

The density of states (DOS) and projected density of states (PDOS) for the relaxed structures were obtained using the tetrahedron method with Blöchl et al. corrections [19] and a KSPACING of 0.3. For all the systems, DFT + U [20] calculations were performed to take into account the on-site Coulomb interaction. A U value of 5 eV was used for d orbitals [21]. Electron localization function (ELF) [22–26] images and structure images were obtained using the Vaspview software and ChemCraft 1.6 [27], respectively.

3. Results and Discussion

3.1. Elemental Analysis. The elemental composition of the samples was determined using X-ray fluorescence spectroscopy (XRF) to measure I and Pb and the CHNS technique to determine C, H, and N. The results of the weight

TABLE 1: Weight and atomic percentage values for the elements in the samples prepared, obtained by means of XRF and CHNS technique.

	Sample, $(A)_x(MA)_{1-x}PbI_3$				
	$x = 0.00$	$x = 0.25$	$x = 0.50$	$x = 0.75$	$x = 1.00$
Wt% C	1.95	1.42	1.01	0.55	—
Wt% H	0.97	0.90	0.83	0.78	0.69
Wt% N	2.29	2.26	2.25	2.31	2.35
Wt% I	61.41	61.81	62.12	62.42	62.78
Wt% Pb	33.38	33.61	33.79	33.94	34.18
At% C	8.4	6.5	4.9	2.8	—
At% H	49.9	49.2	48.0	47.4	45.5
At% N	8.4	8.8	9.3	10.0	11.1
At% I	25.0	26.6	28.3	29.9	32.6
At% Pb	8.3	8.9	9.4	9.9	10.9
x_{real}	0.00	0.27	0.48	0.72	1.00

percentages obtained are shown in Table 1, which also shows the atomic percentage calculated for each element. It is possible to observe only small deviations with regard to the nominal composition (see Experimental Section). To enhance understanding, in the discussion of the results the samples will be identified by the nominal value of x.

3.2. X-Ray Diffraction. Figure 1 shows the XRD patterns for the samples synthesized. The diffractogram for the sample with $x = 0.00$, without NH_4^+, shows the typical peaks of the reflections of the planes of a tetragonal structure (*I4/mcm* space group), which has been reported for $MAPbI_3$ perovskite [28–32]. In addition, the typical peaks for this perovskite structure show the most intense reflections at approximately 14°, 28°, and 31°, these being two double peaks. A peak at about 23.5° is assigned to the reflection plane (211) of the tetragonal perovskite structure mentioned and is the main difference with the cubic perovskite structure (*Pm3m* space group) that is also found in this kind of hybrid perovskites [28]. Thus, the presence of perovskite cubic phase is negligible in our samples. Also, Figure 1 shows that the typical tetragonal structure is maintained in the patterns for the samples with x up to 0.75, but also in these cases a crystallinity loss is observed in the XRD patterns. Not only is the presence of tetragonal perovskite observed in the samples where some amount of ammonium iodide is added, but also other peaks are observed. So, the incorporation of ammonium groups into the tetragonal perovskite structure leads to a dramatic loss of the crystallinity of the perovskite phase and to the presence of other phases.

The formation of the perovskite structure is estimated on the basis of two factors: Goldschmidt's tolerance factor (t) and the "octahedral factor" (μ). Goldschmidt's factor is commonly used for the analysis of the formation of perovskite structures and is estimated for the ABX_3 system according to $t = (r_A + r_X)/2^{1/2}(r_B + r_X)$, where r_A, r_X, and r_B are the effective ionic radii of A, X, and B ions, that is $[CH_3NH_3]^+$ or NH_4^+, I^-, and Pb^{2+} in our case [33]. The "octahedral factor" is calculated according to $\mu = r_B/r_X$ [34, 35]. Thus, according to Goldschmidt's factor, the perovskite structure is formed for values in the 0.75–1.00 range. If $t = 1$, the
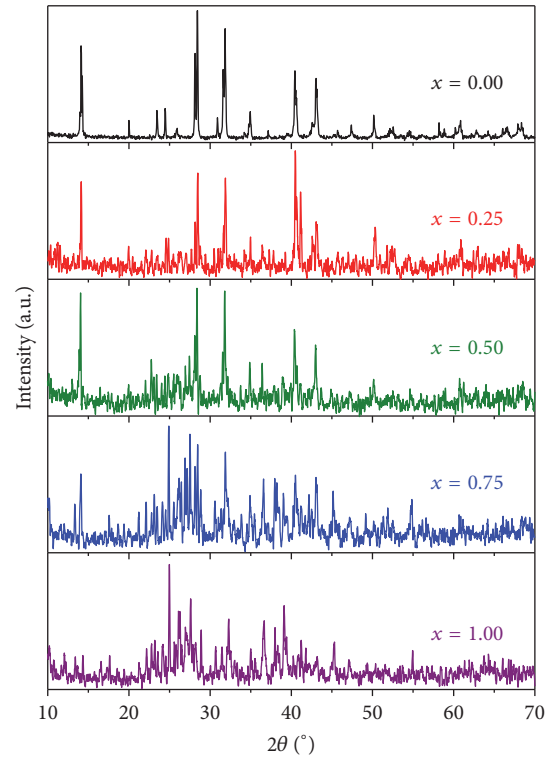
FIGURE 1: XRD patterns for the samples synthesized, $(A)_x(MA)_{1-x}PbI_3$.

ideal cubic perovskite structure would be formed, while for values below 1 octahedral distortions are obtained [35]. For halide-based perovskites, the usual t values are in the 0.813–1.107 range, while the "octahedral factor" is greater than 0.442 in these cases [35]. These two factors were used to analyse the structures of $MAPbI_3$ and $APbI_3$. The effective ionic radius values of NH_4^+, I^-, and Pb^{2+} were taken from the literature [36, 37]. The values are 1.5, 2.2, and 1.19 Å for NH_4^+, I^-, and Pb^{2+}, respectively. In turn, the effective ionic radius of $[CH_3NH_3]^+$ was calculated according to a rigid sphere model with free rotation of its centre of mass, as reported
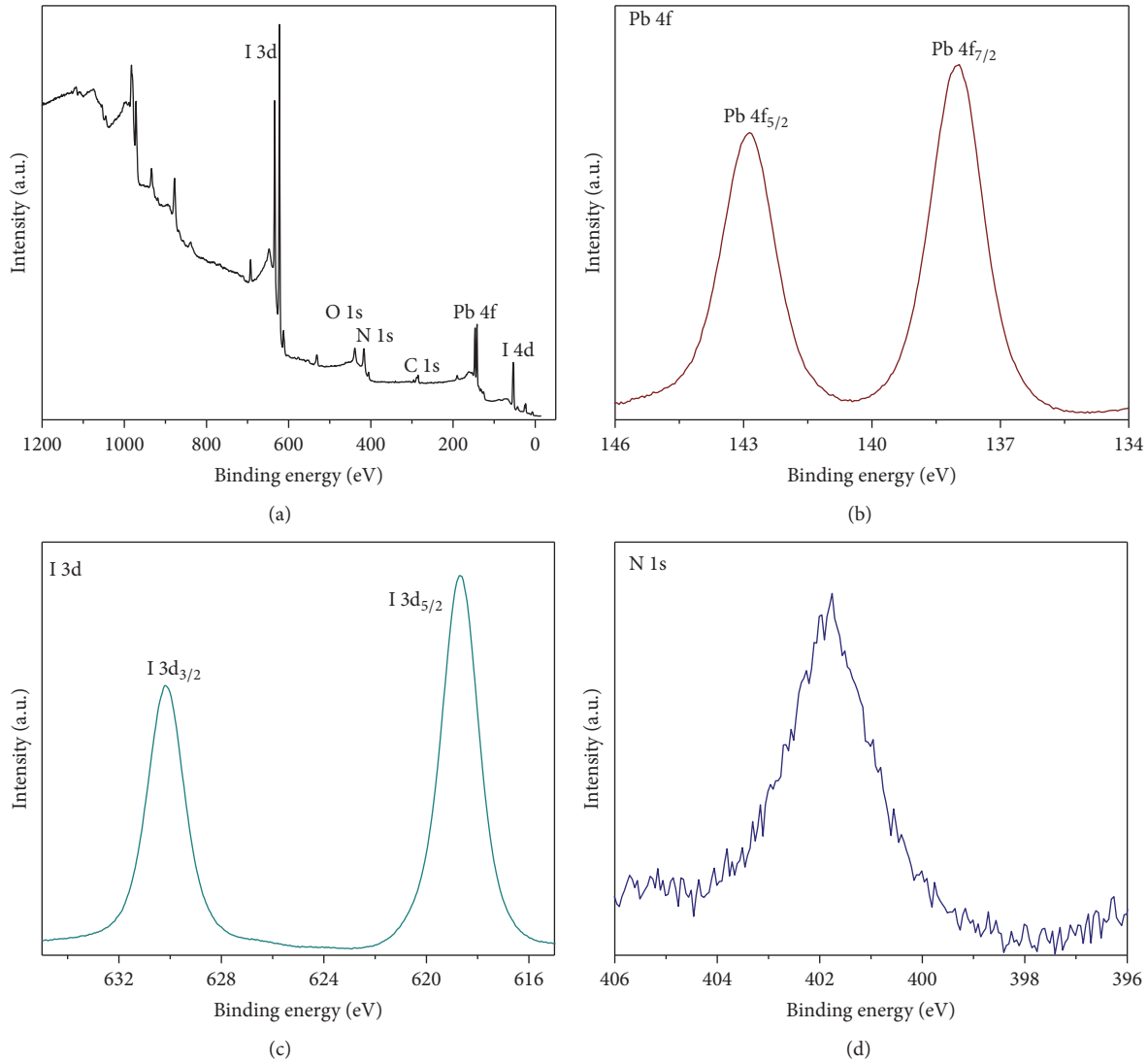
(a)

(b)

(c)

(d)

FIGURE 2: X-ray photoelectron spectra: (a) general; (b) Pb 4f; (c) I 3d; and (d) N 1s, for the sample with $x = 0.50$.

in the literature [38]. The value obtained is 1.74 Å. Thus, the values for t and μ are 0.822 and 0.541 for MAPbI$_3$ and 0.772 and 0.541 for APbI$_3$. Thus, the MAPbI$_3$ system fulfils both conditions, which is in accordance with the formation of tetragonal perovskite structure observed in the XRD patterns for this sample. On the other hand, the APbI$_3$ system shows a suitable "octahedral factor" because of the fact that these ions are the same as that for MAPbI$_3$. But, Goldschmidt's factor for APbI$_3$ ($t = 0.772$) is lower than the usual limit value for halide-based perovskites ($t = 0.813$). This is in line with the results obtained using XRD, which show how the formation of perovskite structure decreases when the proportion of ammonium ion in the samples increases.

3.3. X-Ray Photoelectron Spectroscopy. X-ray photoelectron spectra for sample with $x = 0.5$ were acquired to analyse the oxidation states and the bonding states of the elements in the samples. Figure 2(a) shows the general spectra of the sample $x = 0.5$ with a perovskite structure and the basic

assignment of the peaks found. Different zones in the spectra were recorded in detail for analysis. Figure 2(b) shows the Pb 4f spectra of the samples. The binding energy (BE) for the Pb 4f$_{7/2}$ was around 138.0 eV, which is coherent with results reported previously [39, 40]. Also, the spectra for Pb 4f show spin-orbit components well-separated. This separation was around 4.9 eV, which is typical for Pb^{2+}. On the other hand, Figure 2(c) shows the I 3d spectrum. Also, the spectra show well-separated spin-orbit components with a separation of about 11.5 eV, which is coherent with the results reported for I$^-$ [39]. Also, Figure 2(d) shows the N 1s spectrum. The signal for N 1s appears at about 402 eV, and the signal shows low signal/noise ratio probably due to the lower amount of N in the sample with $x = 0.5$.

Therefore, the results from XPS show the typical spectra of Pb 4f, I 3d, and N 1s for tetragonal perovskite.

3.4. UV-vis Spectroscopy. The optical band gap for the samples synthesized was estimated from UV-vis spectra in diffuse
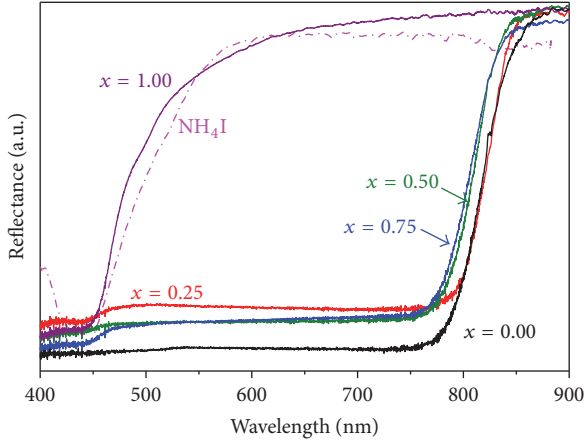
FIGURE 3: UV-vis spectra for the samples synthesized and for commercial NH_4I.

TABLE 2: Band gap values for the samples $A_x(MA)_{1-x}PbI_3$ synthesized.

Sample, x	E_g/eV
0.00	1.54
0.25	1.54
0.50	1.56
0.75	1.56
1.00	2.65

reflectance mode. Figure 3 shows UV-vis spectra obtained for the samples synthesized. From these spectra, the presence of tetragonal phase is observed up to values of x of 0.75, which is coherent with XRD results. The sample with $x = 1$ is clearly different, probably because of the fact that tetragonal perovskite is not obtained. This sample has an absorption band at shorter wavelengths than the sample with $x = 0.00$, that is, $MAPbI_3$. The spectrum for the sample with $x = 1.00$ can be compared with the spectrum obtained for commercial NH_4I used as reagent in the synthesis. It is possible to observe the presence of NH_4I without reacting. So, this is coherent with XRD results.

The band gap of the samples can be estimated from the spectra registered. The Kubelka-Munk formulism from the diffuse reflectance measurements is calculated according to $(\alpha/S) = F(R) = [(1 - R)^2]/2R$ [41], where R is the percentage of reflected light and α and S are the absorption and the scattering coefficients. The Tauc plot relates the band gap and the incident photon energy, and for direct transitions it is given by $[F(R)h\nu]^2 = A(h\nu - E_g)$ [42, 43], where $h\nu$ is the incident photon energy, A is a constant depending on the transition probability, and E_g is the band gap. So, the band gap values were estimated and are shown in Table 2. It is possible to observe that the samples where tetragonal perovskite is formed show similar band gap values. A slight increase is observed for samples with $x = 0.5$ and 0.75. For the sample with $x = 1$, a drastic increase of the band gap is obtained.

3.5. Theoretical Analysis of $(A)_x(MA)_{1-x}PbI_3$. From the results of the experimental characterization, theoretical calculations were performed to gain a deeper understanding of the effect of varying the A cation in the ABX_3 structure of $MAPbI_3$ perovskites. Thus, a study was performed in the tetragonal structure of $(A)_x(MA)_{1-x}PbI_3$ with $x = 0.00, 0.25, 0.50, 0.75,$ and 1.00.

Figure 4 shows the local geometry for the most stable configuration of the optimized perovskite structures when MA^+ were substituted by A^+. For the purpose of comparison, Figure 4 also includes the $MAPbI_3$ structure in tetragonal phase. As it can be seen in Figure 4 the substitution of MA^+ by A^+ ions caused distortions in the structure. The most striking changes are produced for $(A)_{0.75}(MA)_{0.25}PbI_3$ and $APbI_3$ structures. As an example, the structural distortion is clearly reflected in the variation in the Pb-I-Pb angles of the central plane view shown in Figure 4 when compared with the $MAPbI_3$ structure (Table 3). As shown in Table 3 the α, β, γ, and δ angles decrease when A^+ is included in the structure and substitutes the MA^+. The $(A)_{0.25}(MA)_{0.75}PbI_3$ structure is the one that remains the most similar to the $MAPbI_3$ perovskite followed by $(A)_{0.5}(MA)_{0.5}PbI_3$ (Table 3). Thus, it is understandable that $(A)_{0.25}(MA)_{0.75}PbI_3$ and $(A)_{0.50}(MA)_{0.50}PbI_3$ were formed experimentally maintaining the tetragonal phase, while the $(A)_{0.75}(MA)_{0.25}PbI_3$ and $APbI_3$ structures present variation of *c.a.* 9–15° in the angles when compared to $MAPbI_3$ perovskite (Table 3), which means a structural tension that makes its experimental formation difficult. Therefore our results are concordant with those obtained experimentally.

The changes in the band gap for the $(A)_x(MA)_{1-x}PbI_3$ ($x = 0.00, 0.25, 0.50, 0.75,$ and 1.00) structures were analysed by means of DOS (Figure 5). As can be seen in Figure 5 the bad gap increases with the proportion of A^+ ions when compared with $MAPbI_3$ perovskite. In turn, the gap for $(A)_{0.25}(MA)_{0.75}PbI_3$ structure is slightly greater than the gap for $MAPbI_3$ perovskite. Thus, both the geometrical study and the DOS analysis indicate that $(A)_{0.25}(MA)_{0.75}PbI_3$ structure has an appropriate percentage of A^+ and MA^+ ions for being effective for its application in solar cells.

3.6. Theoretical Analysis of $A_{0.25}MA_{0.75}Pb_{1-x}Cd_xI_3$. From the results expounded above, the $A_{0.25}MA_{0.75}PbI_3$ perovskite was selected for exploring theoretically the changes in the structural and electronic properties of the material when the Pb is substituted by Cd. This metal was selected because it is known to decrease the band gap in $MAPbI_3$ perovskites [6, 38] when it is used in B position as an alternative to Pb. Thus, an analysis was performed into the effect of increasing the concentration of Cd on the structural and electronic properties of $(A)_{0.25}(MA)_{0.75}Pb_{1-x}Cd_xI_3$ with $x = 0.00, 0.25, 0.50, 0.75,$ and 1.00.

The theoretical results show that the incorporation of Cd^{2+} ions produced changes when compared with the $(A)_{0.25}(MA)_{0.75}PbI_3$ perovskite. The local geometry for the most stable configuration of the optimized structures is shown in Figure 6. As an example, the Pb-I-Cd and Cd-I-Cd angles of the cut corresponding with the front face of the tetragonal structures as indicated in Figure 6 are shown in
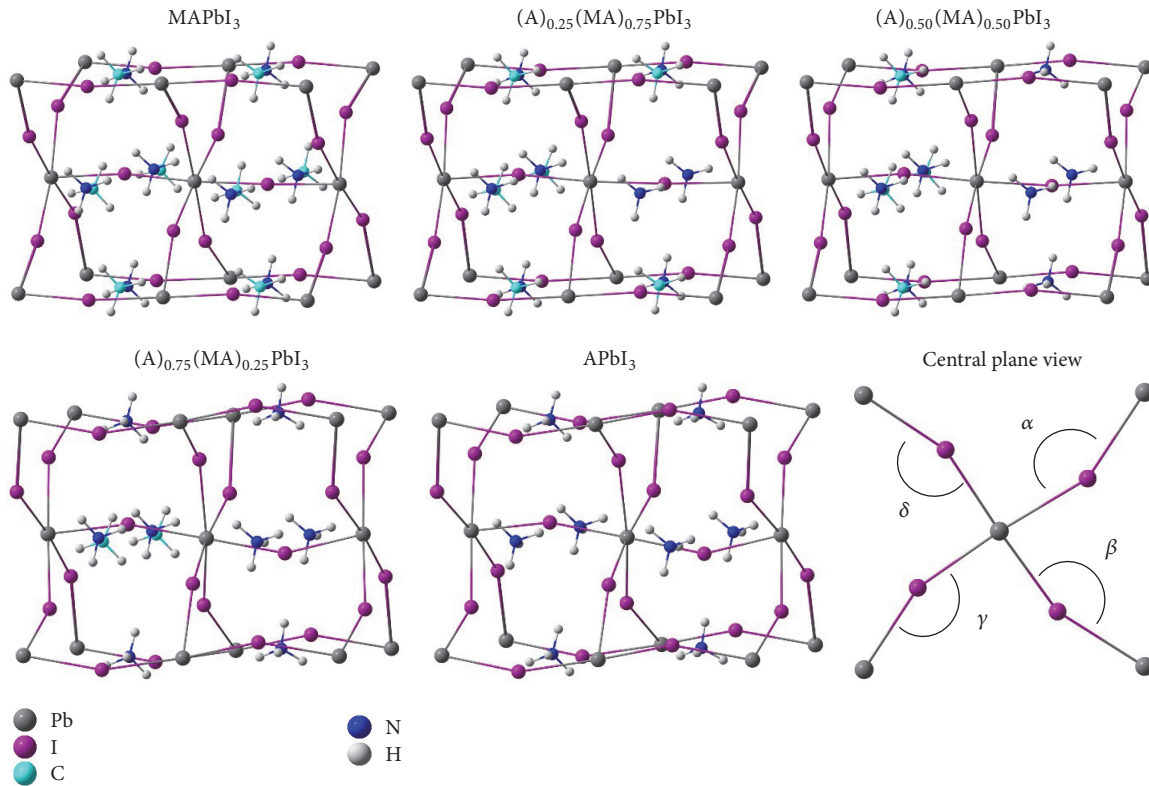
MAPbI$_3$

(A)$_{0.25}$(MA)$_{0.75}$PbI$_3$

(A)$_{0.50}$(MA)$_{0.50}$PbI$_3$

(A)$_{0.75}$(MA)$_{0.25}$PbI$_3$

APbI$_3$

Central plane view

- Pb
- I
- C
- N
- H

FIGURE 4: The local geometry for tetragonal structure of A$_x$(MA)$_{1-x}$PbI$_3$ with x = 0.00, 0.25, 0.50, 0.75, and 1.00.
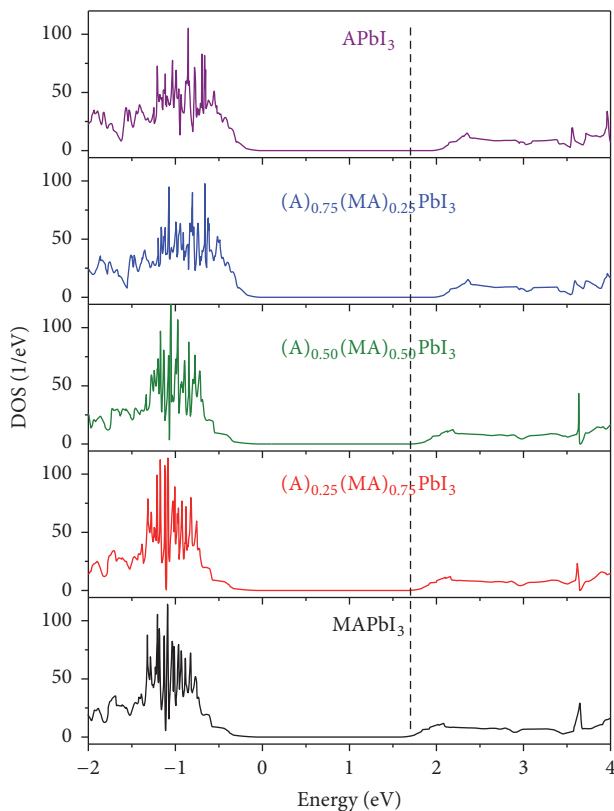

FIGURE 5: Total DOS for tetragonal perovskite structures analysed.

Table 4. As Table 4 shows, η and μ angles increase in accordance with the concentration of Cd, reaching their highest values in (A)$_{0.25}$(MA)$_{0.75}$CdI$_3$. The χ angle hardly changes when compared with the same angle for A$_{0.25}$MA$_{0.75}$PbI$_3$ while σ decreases when the concentration of Cd increases. In addition, it is also observed that, generally, the Cd-I distances are shorter compared with the Pb-I ones (*c.a.* 5–7%). Thus, the ELF plot in 2D corresponding to the Cd-I and Pb-I interactions for the (A)$_{0.25}$(MA)$_{0.75}$Pb$_{0.75}$Cd$_{0.25}$I$_3$ geometry is represented in Figure 6 as an example of how the contour plot for Pb is different from that of Cd. Figure 6 shows that the outlines of the ELF for I and Pb almost overlap by means of slight electron localization (sky blue colour) that provides more stability to the Pb-I interaction, while the introduction of Cd produces directionality in the outlines of the electron localization of I towards Cd, which explains the shorter Cd-I distances. These results lead us to believe that the structural tensions in the theoretical structures (A)$_{0.25}$(MA)$_{0.75}$Pb$_{0.25}$Cd$_{0.75}$I$_3$ and (A)$_{0.25}$(MA)$_{0.75}$CdI$_3$ are greater than those in the structures with low concentrations of Cd^{2+} ions.

The electronic structure in terms of DOS associated with (A)$_{0.25}$(MA)$_{0.75}$Pb$_{1-x}$Cd$_x$I$_3$ (x = 0.00, 0.25, 0.50, 0.75, and 1.00) structures is shown in Figure 7. The DOS analysis of Figure 7 shows the band gap decreases with the concentration of Cd. For clarity purposes in Figure 7 dotted lines showing the narrowing of the band gap between the valence band (VB) and the conduction band (CB) upon increasing the
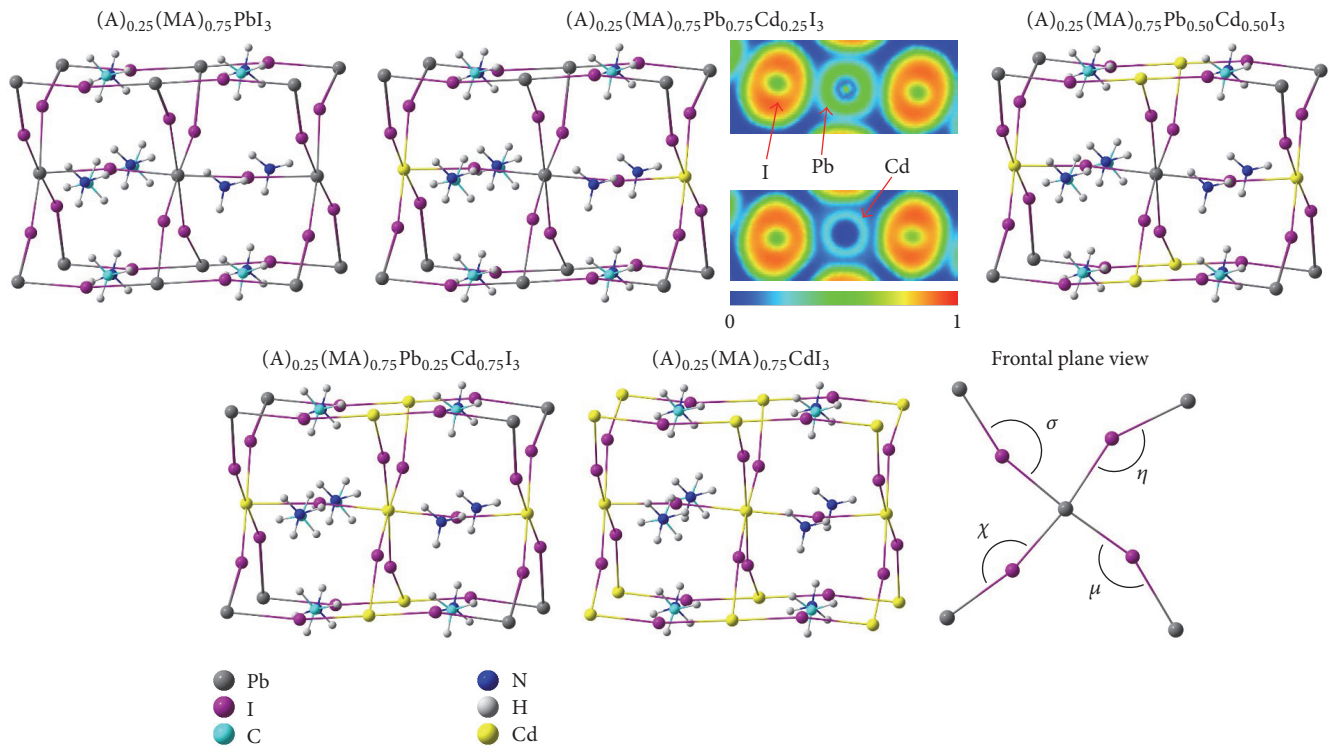
FIGURE 6: The local geometry for the tetragonal $A_{0.25}MA_{0.75}Pb_{1-x}Cd_xI_3$ perovskite with x = 0.00, 0.25, 0.50, 0.75, and 1.00. ELF 2D contour plots for Cd-I and Pb-I interactions are included for the $(A)_{0.25}(MA)_{0.75}Pb_{0.75}Cd_{0.25}I_3$ structure.
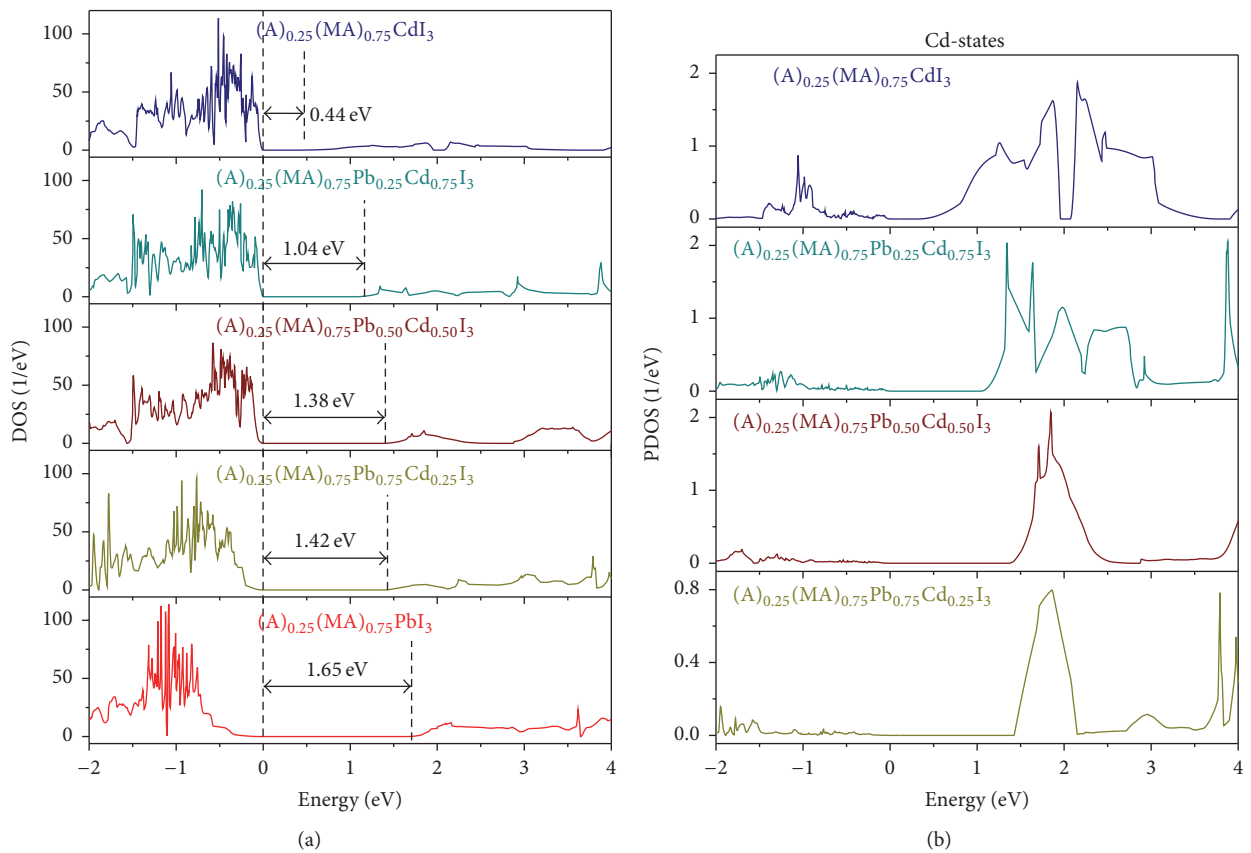

FIGURE 7: Total DOS and Cd projected s-states for tetragonal perovskite structures analysed.

TABLE 3: Geometrical parameters, identified in Figure 4, of the structures studied.

Structure	α	β	γ	δ
$MAPbI_3$	158.35	157.11	155.03	156.52
$(A)_{0.25}(MA)_{0.75}PbI_3$	158.17	157.06	154.36	156.73
$(A)_{0.50}(MA)_{0.50}PbI_3$	156.37	155.54	153.73	156.45
$(A)_{0.75}(MA)_{0.25}PbI_3$	146.35	142.08	148.84	148.04
$APbI_3$	146.22	142.80	147.57	147.46

TABLE 4: Geometrical parameters, identified in Figure 6, of the structures studied.

Structure	η	μ	χ	σ
$(A)_{0.25}(MA)_{0.75}PbI_3$	148.48	155.86	166.75	161.97
$(A)_{0.25}(MA)_{0.75}Pb_{0.75}Cd_{0.25}I_3$	150.17	158.11	166.51	158.38
$(A)_{0.25}(MA)_{0.75}Pb_{0.50}Cd_{0.50}I_3$	149.98	158.90	166.64	157.33
$(A)_{0.25}(MA)_{0.75}Pb_{0.25}Cd_{0.75}I_3$	150.39	159.99	165.76	157.28
$(A)_{0.25}(MA)_{0.75}CdI_3$	150.95	158.82	166.12	158.19

concentration of Cd have been included. Previous studies with $MAPbI_3$ perovskites have shown that Cd d-states contribute to the edge of the valence band while the s-states of Cd contribute to the origin of the conduction band [6, 38]. Thus, the contribution of Cd s-states is also included in Figure 7 and it is shown that the contribution of the s-states of the Cd to the origin of the CB plays a fundamental role in the decrease in the band gap, as reported elsewhere [38]. In addition, our theoretical results let us to conclude that structures with a lower proportion of Cd, such as $(A)_{0.25}(MA)_{0.75}Pb_{0.75}Cd_{0.25}I_3$ and $(A)_{0.25}(MA)_{0.75}Pb_{0.50}Cd_{0.50}I_3$, with lesser structural tension than those with higher proportion would be of interest for being used in photovoltaic devices.

4. Conclusions

In this work, the synthesis of $(A)_x(MA)_{1-x}PbI_3$ (x = 0.00; 0.25; 0.50; 0.75; 1.00) tetragonal perovskite was performed. From the experimental characterization, the presence of perovskite cubic phase is negligible in our samples. Also, a crystallinity loss in the samples when NH_4^+ cations were incorporated was observed, and the $APbI_3$ perovskite was not found. So, the incorporation of ammonium groups into the tetragonal perovskite structure lead to a dramatic loss of the crystallinity of the perovskite phase and to the presence of other phases. Also, Goldschmidt's factor for $APbI_3$ (t = 0.772) is lower than the usual limit value for halide-based perovskites (t = 0.813). This is in line with the results obtained using XRD, which show how the formation of perovskite structure decreases when the proportion of ammonium ion in the samples increases. On the other hand, the results from XPS show the typical spectra of Pb 4f, I 3d, and N 1s for tetragonal perovskite. So, the less formation of perovskite phase when NH_4^+ is incorporated is due to geometrical factors and not from changes in the chemical state bonding of the ions in the structure. Also, UV-vis spectra are coherent with XRD results. The spectra for the sample with x = 1.00 are similar to that of commercial NH_4I, so $APbI_3$ was not formed.

In turn, the band gap energy was estimated. The samples where tetragonal perovskite is formed show similar band gap values. A slight increase is observed for samples with x = 0.5 and 0.75. For the sample with x = 1, a drastic increase of the band gap is obtained.

DFT calculations show that the tendency followed by the band gap values calculated by means of DOS for $A_x(MA)_{1-x}PbI_3$ with x = 0.00, 0.25, 0.50, 0.75, and 1.00 tetragonal perovskite was in agreement with that obtained experimentally. In this sense, the DOS and structural analysis indicate that $(A)_{0.25}(MA)_{0.75}PbI_3$ structure has an appropriate percentage of A^+ and MA^+ ions for being effective for its application in solar cells. $(A)_{0.25}(MA)_{0.75}PbI_3$ was selected for the substitution of Pb by Cd and structural tensions were observed in the structures with high concentrations of Cd^{2+} ions. The band gap decreases when the concentration of Cd increases. The projected density of states focused on the Cd s-states shows the important role played by s-states of Cd in narrowing the band gap between the VB and CB. Finally, from the DOS and structural analysis it can be concluded that the structures with the lowest Cd proportion with lesser structural tensions, such as $(A)_{0.25}(MA)_{0.75}Pb_{0.75}Cd_{0.25}I_3$ and $(A)_{0.25}(MA)_{0.75}Pb_{0.50}Cd_{0.50}I_3$, would be of interest for their application in solar cells.

Competing Interests

The authors declare that there is no conflict of interests regarding the publication of this paper.
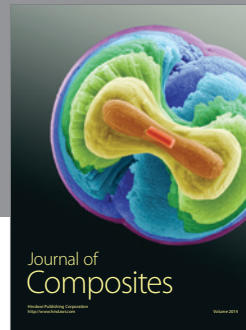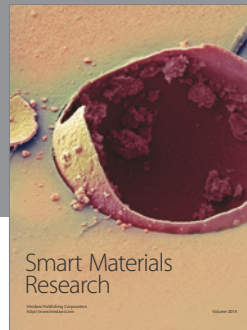
Acknowledgments

References

[1] M. Grätzel, "The light and shade of perovskite solar cells," *Nature Materials*, vol. 13, no. 9, pp. 838–842, 2014.

[2] D. Bi, W. Tress, M. I. Dar et al., "Efficient luminescent solar cells based on tailored mixed-cation perovskites," *Science Advances*, vol. 2, no. 1, Article ID e1501170, 2016.

[3] N. J. Jeon, J. H. Noh, W. S. Yang et al., "Compositional engineering of perovskite materials for high-performance solar cells," *Nature*, vol. 517, no. 7535, pp. 476–480, 2015.

[4] N. Pellet, P. Gao, G. Gregori et al., "Mixed-organic-cation perovskite photovoltaics for enhanced solar-light harvesting," *Angewandte Chemie - International Edition*, vol. 53, no. 12, pp. 3151–3157, 2014.

[5] M. Graetzel, R. A. J. Janssen, D. B. Mitzi, and E. H. Sargent, "Materials interface engineering for solution-processed photovoltaics," *Nature*, vol. 488, no. 7411, pp. 304–312, 2012.

[6] J. Navas, A. Sánchez-Coronilla, J. J. Gallardo et al., "New insights into organic–inorganic hybrid perovskite $CH_3NH_3PbI_3$ nanoparticles. An experimental and theoretical study of doping in Pb^{2+} sites with Sn^{2+}, Sr^{2+}, Cd^{2+} and Ca^{2+}," *Nanoscale*, vol. 7, no. 14, pp. 6216–6229, 2015.

[7] Y. Ogomi, A. Morita, S. Tsukamoto et al., "CH3NH3SnxPb(1-x)I3 perovskite solar cells covering up to 1060 nm," *Journal of Physical Chemistry Letters*, vol. 5, no. 6, pp. 1004–1011, 2014.

[8] P. Umari, E. Mosconi, and F. De Angelis, "Relativistic GW calculations on $CH_3NH_3PbI_3$ and $CH_3NH_3SnI_3$ perovskites for solar cell applications," *Scientific Reports*, vol. 4, article 4467, 2014.

[9] S.-R. Jang, K. Zhu, M. J. Ko et al., "Voltage-enhancement mechanisms of an organic dye in high open-circuit voltage solid-state dye-sensitized solar cells," *ACS Nano*, vol. 5, no. 10, pp. 8267–8274, 2011.

[10] H.-S. Kim, C.-R. Lee, J.-H. Im et al., "Lead iodide perovskite sensitized all-solid-state submicron thin film mesoscopic solar cell with efficiency exceeding 9%," *Scientific Reports*, vol. 2, article no. 591, 2012.

[11] G. Kresse and J. Furthmüller, "Efficiency of ab-initio total energy calculations for metals and semiconductors using a plane-wave basis set," *Computational Materials Science*, vol. 6, no. 1, pp. 15–50, 1996.

[12] G. Kresse and J. Furthmüller, "Efficient iterative schemes for ab initio total-energy calculations using a plane-wave basis set," *Physical Review B*, vol. 54, no. 16, pp. 11169–11186, 1996.

[13] G. Kresse and J. Hafner, "Ab initio molecular dynamics for liquid metals," *Physical Review B*, vol. 47, no. 1, pp. 558–561, 1993.

[14] G. Kresse and J. Hafner, "Ab initio molecular-dynamics simulation of the liquid-metalamorphous- semiconductor transition in germanium," *Physical Review B*, vol. 49, no. 20, pp. 14251–14269, 1994.

[15] P. E. Blöchl, "Projector augmented-wave method," *Physical Review B*, vol. 50, no. 24, pp. 17953–17979, 1994.

[16] G. Kresse and D. Joubert, "From ultrasoft pseudopotentials to the projector augmented-wave method," *Physical Review B*, vol. 59, no. 3, pp. 1758–1775, 1999.

[17] J. P. Perdew, K. Burke, and M. Ernzerhof, "Generalized gradient approximation made simple," *Physical Review Letters*, vol. 77, no. 18, pp. 3865–3868, 1996.

[18] A. Poglitsch and D. Weber, "Dynamic disorder in methylammoniumtrihalogenoplumbates (II) observed by millimeter-wave spectroscopy," *The Journal of Chemical Physics*, vol. 87, no. 11, pp. 6373–6378, 1987.

[19] P. E. Blöchl, O. Jepsen, and O. K. Andersen, "Improved tetrahedron method for Brillouin-zone integrations," *Physical Review B*, vol. 49, no. 23, pp. 16223–16233, 1994.

[20] S. L. Dudarev, G. A. Botton, S. Y. Savrasov, C. J. Humphreys, and A. P. Sutton, "Electron-energy-loss spectra and the structural stability of nickel oxide: an LSDA+U study," *Physical Review B*, vol. 57, no. 3, pp. 1505–1509, 1998.

[21] E. Menéndez-Proupin, A. Amézaga, and N. Cruz Hernández, "Electronic structure of CdTe using GGA+U^{SIC}," *Physica B: Condensed Matter*, vol. 452, pp. 119–123, 2014.

[22] A. D. Becke and K. E. Edgecombe, "A simple measure of electron localization in atomic and molecular systems," *The Journal of Chemical Physics*, vol. 92, no. 9, pp. 5397–5403, 1990.

[23] A. Savin, A. D. Becke, J. Flad, R. Nesper, H. Preuss, and H. G. von Schnering, "A new look at electron localization," *Angewandte Chemie International Edition in English*, vol. 30, no. 4, pp. 409–412, 1991.

[24] A. Savin, O. Jepsen, J. Flad, O. K. Andersen, H. Preuss, and H. G. von Schnering, "Electron localization in solid–state structures of the elements: the diamond structure," *Angewandte Chemie International Edition in English*, vol. 31, no. 2, pp. 187–188, 1992.

[25] B. Silvi and C. Gatti, "Direct space representation of the metallic bond," *The Journal of Physical Chemistry A*, vol. 104, no. 5, pp. 947–953, 2000.

[26] B. Silvi and A. Savin, "Classification of chemical-bonds based on topological analysis of electron localization functions," *Nature*, vol. 371, no. 6499, pp. 683–686, 1994.

[27] http://www.chemcraftprog.com/.

[28] T. Baikie, Y. Fang, J. M. Kadro et al., "Synthesis and crystal chemistry of the hybrid perovskite (CH3NH3) PbI3 for solid-state sensitised solar cell applications," *Journal of Materials Chemistry A*, vol. 1, no. 18, pp. 5628–5641, 2013.

[29] J. Burschka, N. Pellet, S.-J. Moon et al., "Sequential deposition as a route to high-performance perovskite-sensitized solar cells," *Nature*, vol. 499, no. 7458, pp. 316–319, 2013.

[30] A. Kojima, K. Teshima, Y. Shirai, and T. Miyasaka, "Organometal halide perovskites as visible-light sensitizers for photovoltaic cells," *Journal of the American Chemical Society*, vol. 131, no. 17, pp. 6050–6051, 2009.

[31] M. M. Lee, J. Teuscher, T. Miyasaka, T. N. Murakami, and H. J. Snaith, "Efficient hybrid solar cells based on meso-superstructured organometal halide perovskites," *Science*, vol. 338, no. 6107, pp. 643–647, 2012.

[32] J. H. Noh, S. H. Im, J. H. Heo, T. N. Mandal, and S. I. Seok, "Chemical management for colorful, efficient, and stable inorganic-organic hybrid nanostructured solar cells," *Nano Letters*, vol. 13, no. 4, pp. 1764–1769, 2013.

[33] V. M. Goldschmidt, "Crystal structure and chemical correlation," *Berichte der Deutschen Chemischen Gesellschaft*, vol. 60, no. 5, pp. 1263–1296, 1927.

[34] L. M. Feng, L. Q. Jiang, M. Zhu, H. B. Liu, X. Zhou, and C. H. Li, "Formability of ABO_3 cubic perovskites," *Journal of Physics and Chemistry of Solids*, vol. 69, no. 4, pp. 967–974, 2008.

[35] C. Li, X. Lu, W. Ding, L. Feng, Y. Gao, and Z. Guo, "Formability of ABX_3 (X = F, Cl, Br, I) halide perovskites," *Acta Crystallographica Section B: Structural Science*, vol. 64, no. 6, pp. 702–707, 2008.

[36] R. D. Shannon, "Revised effective ionic-radii and systematic studies of interatomic distances in halides and chalcogenides," *Acta Crystallographica Section A*, vol. 32, no. 5, pp. 751–767, 1976.

[37] T. M. W. J. Bandara, W. J. M. J. S. R. Jayasundara, M. A. K. L. Dissanayake, M. Furlani, I. Albinsson, and B.-E. Mellandera, "Effect of cation size on the performance of dye sensitized nanocrystalline TiO2 solar cells based on quasi-solid state PAN electrolytes containing quaternary ammonium iodides," *Electrochimica Acta*, vol. 109, pp. 609–616, 2013.

[38] J. Navas, A. Sanchez-Coronilla, J. J. Gallardo et al., "Revealing the role of Pb^{2+} in the stability of organic-inorganic hybrid perovskite $CH_3NH_3Pb_{1-x}Cd_xI_3$: an experimental and theoretical study," *Physical Chemistry Chemical Physics*, vol. 17, no. 37, pp. 23886–23896, 2015.

[39] A. V. Naumkin, A. Kraut-Vass, S. W. Gaarenstroom, and C. J. Powell, *NIST Standard Reference Database 20, Version 4.1*, NIST, Gaithersburg, Md, USA, 2012.

[40] Z. Zheng, S. Wang, D. Li et al., "Morphology-controlled synthesis of lead iodine compounds from lead foils and iodine," *Journal of Crystal Growth*, vol. 308, no. 2, pp. 398–405, 2007.

[41] L. F. Gate, "Comparison of the photon diffusion model and Kubelka-Munk equation with the exact solution of the radiative transport equation," *Applied Optics*, vol. 13, no. 2, pp. 236–238, 1974.

[42] J. Navas, A. Sanchez-Coronilla, T. Aguilar, N. C. Hernandez, D. M. de los Santos, and J. Sanchez-Marquez, "Experimental and theoretical study of the electronic properties of Cu-doped anatase TiO_2," *Physical Chemistry Chemical Physics*, vol. 16, pp. 3835–3845, 2014.

[43] N. Serpone, D. Lawless, and R. Khairutdinov, "Size effects on the photophysical properties of colloidal anatase TiO2 particles: size quantization or direct transitions in this indirect semiconductor?" *Journal of Physical Chemistry*, vol. 99, no. 45, pp. 16646–16654, 1995.